

Spatial Interpolation of Room Impulse Responses based on Deeper Physics-Informed Neural Networks with Residual Connections

KEN KURATA¹, GEN SATO¹, IZUMI TSUNOKUNI¹, AND YUSUKE IKEDA¹, (Member, IEEE)

¹Tokyo Denki University, 5 Senju-Asahi-Cho, Adachi-ku, Tokyo, JAPAN, 120-8551, Acoustics & Communication Laboratory (e-mail: yusuke.ikeda@mail.dendai.ac.jp)

Corresponding author: Ken Kurata (e-mail: 24fmi09@ms.dendai.ac.jp).

This work was partially supported by JSPS KAKENHI Grant Number 22K12099 and JGC-Saneyoshi Scholarship Foundation. This work has been submitted to the IEEE for possible publication. Copyright may be transferred without notice, after which this version may no longer be accessible.

ABSTRACT The room impulse response (RIR) characterizes sound propagation in a room from a loudspeaker to a microphone under the linear time-invariant assumption. Estimating RIRs from a limited number of measurement points is crucial for sound propagation analysis and visualization. Physics-informed neural networks (PINNs) have recently been introduced for accurate RIR estimation by embedding governing physical laws into deep learning models; however, the role of network depth has not been systematically investigated. In this study, we developed a deeper PINN architecture with residual connections and analyzed how network depth affects estimation performance. We further compared activation functions, including tanh and sinusoidal activations. Our results indicate that the residual PINN with sinusoidal activations achieves the highest accuracy for both interpolation and extrapolation of RIRs. Moreover, the proposed architecture enables stable training as the depth increases and yields notable improvements in estimating reflection components. These results provide practical guidelines for designing deep and stable PINNs for acoustic-inverse problems.

INDEX TERMS Room acoustics, room impulse response estimation, sound field reconstruction, SIREN, residual connections, three-dimensional sound field.

I. INTRODUCTION

The room impulse response (RIR) is a signal that represents the sound propagation in a room from a loudspeaker to a microphone, based on the assumption that the sound field is linear and time invariant. The RIR is utilized for various acoustic fields and applications, including sound field reproduction [1], [2] and sound source localization [3], [4]. Moreover, the early part of the RIR significantly influences the sound localization and timbre impression of the sound source [5].

In applications where spatial variations in sound propagation are essential—such as sound field visualization [6]–[8] and sound field control [9]–[11]—acquiring RIRs over large regions at high spatial densities is crucial for accurately representing the sound field. In particular, the early part of RIR can vary substantially with the measurement position. However, when RIR measurements are required over large

regions or at high spatial densities, it is impractical—in terms of the measurement cost—to physically place microphones at all desired locations. Therefore, various methods have been proposed to estimate the RIRs in a region of interest using measurements from only a limited number of microphones.

One well-known category of approaches is model-based approaches that incorporate compressed sensing (CS) [12], [13]. In CS-based methods, the sound field is represented as a sparse linear combination of physical models, such as plane waves [14] and point sources [15].

For example, the sparse equivalent source method [16], [17] represents the sound field by superposition of sparse point sources. Additionally, in the study by Verburg *et al.*, the sound field was modeled as a superposition of plane waves, assuming that the weights of this superposition were sparse [14]. Furthermore, Koyama *et al.* reconstructed the sound field by modeling direct sound with sparse point

arXiv:2512.22915v1 [eess.AS] 28 Dec 2025

sources and the reverberant component using a combination of sparse plane waves and a low-rank matrix [18].

Another line of research focuses on least-squares-based solutions utilizing kernel ridge regression (KRR) [19]–[21]. Horiuchi *et al.* proposed a method for automatically learning and optimizing the parameters of the kernel function used in sound field estimation directly from measured signals [19]. Ueno *et al.* reported that estimation accuracy was improved by incorporating the Helmholtz equation into the KRR framework [20]. Additionally, in the study by Ribeiro *et al.*, the kernel is defined as the sum of two components: one kernel is designed to capture direct sound and early reflections, and the other to capture reverberation [21].

RIR estimation methods based on deep learning have been rapidly developed in recent years. Convolutional neural networks (CNNs) [22] and generative adversarial networks (GANs) [23] can model the relationship between inputs and outputs, and have been applied to estimate RIRs [24], [25]. Lluís *et al.* proposed a U-Net architecture [26] trained on the sound field data obtained using the Green's function in a rectangular room as a super-resolution task [24]. Fernandez-Grande *et al.* employed a GAN-based approach to estimate RIRs from limited measurement signals, achieving improved estimation accuracy compared to previous plane wave regression methods [25].

However, these data-driven deep learning models require a substantial amount of training data. To address this challenge, physics-informed neural networks (PINNs) [27] have been introduced that incorporate physical laws into their loss functions. A key advantage of PINNs is that they learn an implicit neural representation of a specific sound field by incorporating physical laws, including boundary and initial conditions, rather than learning data structure from large datasets. Furthermore, by constraining network outputs to adhere to the governing partial differential equations (PDEs) that represent physical laws, PINNs are expected to achieve a higher estimation accuracy in solving forward and inverse problems than other deep learning methods. For example, in forward problems, Raissi *et al.* applied PINNs to the Schrödinger and Navier-Stokes equations [27]. Moreover, Alkhadhr *et al.* reported that for the linear wave equation, PINNs achieved comparable accuracy to the finite difference method with approximately half the computation time [28].

Furthermore, several studies have applied PINNs to inverse problems, including estimating RIRs at arbitrary positions from measured RIRs [31]–[34]. In particular, sinusoidal representation networks (SIREN) [29], which employ sinusoidal activation functions in a multilayer perceptron (MLP) [30], are one of the commonly used architectures in PINN-based RIR estimation. SIREN is an effective architecture for learning neural implicit representations of various signals. Specifically, Pezzoli *et al.* compared the PINNs and CS methods and showed that the PINNs method achieved an improvement in RIR estimation accuracy [32]. Furthermore, Olivieri *et al.* demonstrated a three-dimensional sound field reconstruction using PINNs [34]. In these studies, the exper-

iments were conducted using relatively shallow architectures with a limited number of hidden layers.

Increasing the number of network layers generally improves the representational capacity, albeit at the cost of longer training time. This increased capacity can be beneficial in challenging scenarios such as long signals or noisy environments, where shallow networks may not achieve sufficient estimation accuracy. In PINNs, deeper networks often suffer from training instabilities including exploding or vanishing gradients [36]. Consequently, simply increasing the number of layers does not necessarily improve the performance and may even degrade the estimation accuracy.

In recent years, various architectural improvements have been proposed to facilitate deeper neural networks, including residual and densely connected architectures [37], [38]. In the context of PINNs, these ideas have been introduced mainly for forward problems to stabilize the training and enable deeper networks [39]–[41]. Cheng and Zhang introduced ResNet-like blocks into PINNs for fluid dynamics forward problems [39]. ResNet-style skip connections improve trainability by enabling residual learning through additive identity mappings [37]. Jiang *et al.* demonstrated that residual connections combined with element-wise multiplication facilitate deeper PINNs and improve the accuracy of forward problems, such as one-dimensional wave propagation [40].

The application of residual connections to PINNs has also been explored to solve inverse problems. For instance, Tian *et al.* performed wind-field reconstruction using PINNs with an MLP augmented by residual connections [36]. This method achieved robust estimation under noisy conditions, and by mitigating the vanishing gradient problem, it enabled the accurate computation of the governing physical laws.

In addition, residual connections in SIREN-based architectures have been studied to facilitate deeper networks. Lu *et al.* demonstrated that adding residual connections to SIREN stabilized the training and improved the accuracy of the 3D image reconstruction [42]. Based on this architecture, we previously proposed relatively shallow PINNs incorporating SIREN with residual connections for 2D sound fields [43].

However, for inverse problems in PINN-based RIR estimation, the effect of network depth in architectures with residual connections has not been systematically studied. In addition, the relative suitability of activation functions (e.g., tanh vs. sin) for this acoustic-inverse problem remains unclear because direct comparisons are limited. Consequently, it is not yet well understood how increasing depth influences RIR estimation performance and which activation function is most appropriate for the task.

In this study, we investigated the acoustic-inverse problem of RIR estimation in a three-dimensional sound field to address these open questions. To this end, we employed a PINN architecture that combines SIREN with residual connections. We further conducted a direct comparison between SIREN-based and tanh-based PINN architectures across different depths, with and without residual connections, to quantify the effects of activation functions, network depth, and residual

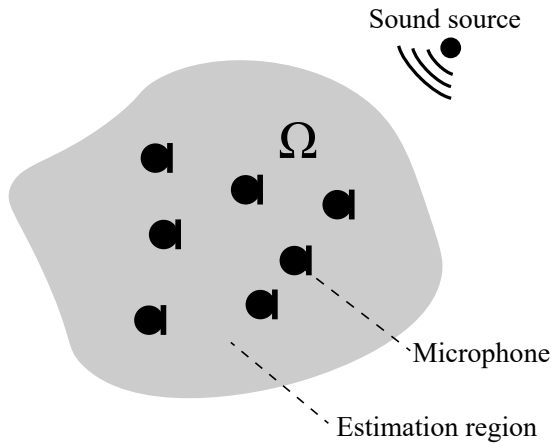


FIGURE 1: Problem of RIR estimation from a limited number of microphones

connections on RIR estimation performance.

The remainder of this paper is organized as follows. Section II explains the problem formulation. Section III introduces the theoretical background and the architecture of the proposed method. Section IV outlines the experimental conditions used to validate the proposed method. Section V demonstrates the effectiveness of the proposed method through simulation results, focusing on the estimation accuracy in both time and frequency domains. Finally, Section VI concludes the paper.

II. PROBLEM FORMULATION

In this study, we estimate the RIRs within a three-dimensional region $\Omega (\subset \mathbb{R}^3)$ that contains neither sound sources nor diffracting objects, as shown in Fig. 1. Under these assumptions, the RIR $h(\mathbf{x}, t)$ at arbitrary position $\mathbf{x} (\in \Omega)$ satisfies the following homogeneous wave equation:

$$\frac{1}{c^2} \frac{\partial^2 h(\mathbf{x}, t)}{\partial t^2} - \nabla^2 h(\mathbf{x}, t) = 0, \quad (1)$$

where c is the speed of sound and ∇ is the gradient.

Let $h(\mathbf{x}_m, t)$ denote the RIR measured at m -th microphone position $\mathbf{x}_m (\in \Omega)$ in time t . We estimate the RIR signal by fitting the measured signals $h(\mathbf{x}_m, t)$ at the measurement points \mathbf{x}_m while enforcing the wave equation at arbitrary points in Ω . Accordingly, the RIR at an arbitrary position \mathbf{x} can be expressed as

$$\hat{h}(\mathbf{x}, t) = \mathcal{U}(\mathbf{x}, t) \quad (2)$$

where the function $\mathcal{U}(\cdot)$ denotes a neural network trained using both the measurement loss and the physics-based constraint in Eq. (1).

Although a room impulse response is generated by an impulsive source and boundary reflections, our reconstruction is formulated on a spatial region Ω that does not include the source position or any obstacles. Hence, within Ω , the field after excitation satisfies the source-free wave equation, while

the influence of the source and room boundaries is implicitly embedded in the observed microphone signals.

In the following sections, both the measurement and evaluation positions are discretized. Accordingly, the RIR at the m -th position is denoted by $h_m(t)$ rather than $h(\mathbf{x}_m, t)$, where the subscript m indexes the spatial location.

III. METHOD

This section provides an overview of PINNs and the proposed method for RIR estimation, specifically to estimate unobserved RIRs from a limited set of measured RIRs. PINNs are well suited to sound-field interpolation because they embed governing equations in the loss function, enabling accurate estimation in the neighborhood of measurement points from limited data.

A. PHYSICS-INFORMED NEURAL NETWORKS (CONVENTIONAL METHOD)

PINNs represent a deep learning methodology that incorporates physical laws into the loss function [27]. Unlike conventional data-driven neural networks, PINNs leverage physical laws to guide the learning process and ensure physically consistent predictions. In acoustics, the wave equation Eq. (1) governs the sound propagation. We incorporate this into the loss function and compute the required second-order derivatives via automatic differentiation.

In the following sections, we describe the conventional PINN framework, first presenting the loss function, and then the network architecture.

1) Loss Functions

For the acoustic-inverse problem, the PINN is trained by minimizing the following loss function, which consists of a data-misfit term at the microphone locations and a governing-equation (wave-equation) residual term:

$$\mathcal{L} = \mathcal{L}_{\text{err}} + \lambda \mathcal{L}_{\text{pde}}, \quad (3)$$

$$\mathcal{L}_{\text{err}} = \frac{1}{\tilde{M}} \sum_{m \in \tilde{\mathcal{M}}} \sum_{v \in \mathcal{T}} \|\hat{h}_m(t_v) - h_m(t_v)\|_2^2, \quad (4)$$

$$\mathcal{L}_{\text{pde}} = \frac{1}{M} \sum_{m \in \mathcal{M}} \sum_{v \in \mathcal{T}} \left\| \frac{1}{c^2} \frac{\partial^2 \hat{h}_m(t_v)}{\partial t_v^2} - \nabla^2 \hat{h}_m(t_v) \right\|_2^2. \quad (5)$$

Here, \mathcal{L}_{err} is defined as the mean squared error (MSE), which quantifies the estimation error between measured signals h_m and estimated signals \hat{h}_m . \mathcal{T} denotes the set of time indices, where t_v represents the v -th time sample. \mathcal{L}_{pde} represents the wave equation residual term. As \mathcal{L}_{pde} approaches zero, the estimated signals \hat{h}_m increasingly satisfy the physical constraints imposed by the wave equation. The balancing parameter λ adjusts the trade-off between the data fidelity and physical consistency. $\tilde{\mathcal{M}}$ is the set of position indices for the measurement positions and \mathcal{M} is the set of position indices for the estimation points. $\tilde{M} = |\tilde{\mathcal{M}}|$ and $M = |\mathcal{M}|$ indicate the number of measurement positions and estimation points, respectively.

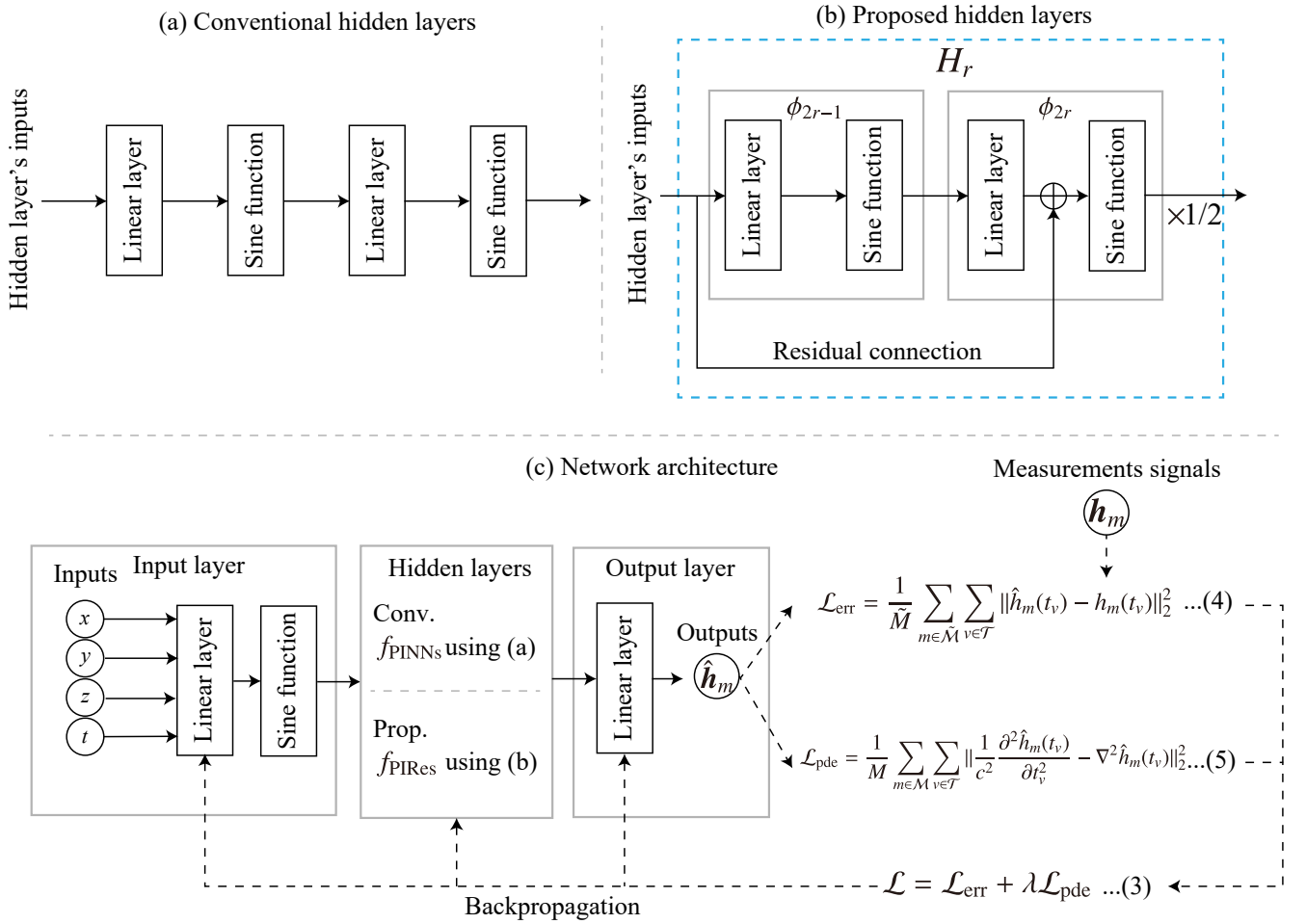


FIGURE 2: (a) Conventional hidden layers architecture. (b) Proposed hidden layers architecture. (c) Network architecture. Inputs are coordinates (x, y, z) and time t . The network is composed of N hidden layers. The loss function is calculated by the output RIRs $\hat{h}_m (m \in \mathcal{M})$ and measured RIRs h_m . The network parameters (\mathbf{w} and \mathbf{b}) are then optimized by minimizing this total loss function, Eq. (3), via backpropagation. \mathcal{M} is the set of indices for the estimation points.

2) Network Architecture

Standard PINNs employ an MLP as an implicit function representation, mapping the spatial coordinates to target field variables [27]. This coordinate-based representation provides a mesh-free, continuous approximation of the target field and enables efficient evaluation of the PDE residual via automatic differentiation.

In this study, the wave-equation residual is computed from the second-order derivatives of the network output. However, common activation functions, such as ReLU and tanh, can be unsuitable when accurate high-order derivatives are required [29]. In particular, ReLU yields piecewise-linear outputs whose second and higher-order derivatives are zero almost everywhere. Although tanh is smooth, its derivatives

can rapidly diminish and may attenuate fine-scale variations during repeated differentiation. To address this issue, we utilize the SIREN [29], an MLP-based architecture that uses a sine function as an activation function, enabling more accurate computation of higher-order derivatives.

The hidden layers of the SIREN network f_{PINNs} can be expressed as a composite function of each network layer ϕ_n as follows:

$$f_{\text{PINNs}}(\mathbf{w}, \mathbf{x}) = (\phi_N \circ \phi_{N-1} \circ \dots \circ \phi_1)(x) \quad (6)$$

$$\phi_n(\mathbf{x}_n) = \sin(\omega_0(\mathbf{x}_n \mathbf{w}_n + \mathbf{b}_n)) \quad (7)$$

where ω_0 , \mathbf{w}_n , and \mathbf{b}_n are the hyperparameters, network weights for the n -th layer, and biases, respectively, and \mathbf{x}_n is the input to the n -th layer, consisting of spatial coordinates

and time. N denotes the total number of hidden layers ϕ . Fig. 2(a) shows the conventional model architecture. The conventional PINNs architecture consists of a stack of fully-connected (linear) layers and activation functions.

Following Sitzmann *et al.* [29], to stabilize the training in the SIREN architecture, the input is normalized to the range $[-1, 1]$, and the weights of each layer are initialized as follows:

$$\mathbf{w}_0 \sim \mathcal{U}(-1/s_0, 1/s_0), \quad (8)$$

$$\mathbf{w}_n \sim \mathcal{U}\left(-\frac{\sqrt{6/s_n}}{\omega_0}, \frac{\sqrt{6/s_n}}{\omega_0}\right), \quad n = 1, 2, 3, \dots, N \quad (9)$$

where s_0 is the input dimension, and s_n is the number of neurons in the n -th hidden layer.

B. PINNS WITH RESIDUAL CONNECTIONS (PROPOSED METHOD)

In general, MLP architectures, including SIREN, are expected to enhance their expressive power as network depth increases. However, simply increasing the number of layers often results in unstable training owing to vanishing and exploding gradients.

To address this issue and achieve stable network training, this study incorporates residual connections into the SIREN. Specifically, we adopt a block structure similar to ResNet-18 [37], which enables deepening by preserving the input information during the learning process. However, to comply with the SIREN requirement that inputs to hidden layers remain within $[-1, 1]$, we introduce additional scaling. After adding the input and output of the hidden layer, we multiply the result by $1/2$ to maintain the values within this range.

As shown in Fig. 2(b), the hidden layers f_{PIRes} can be expressed as a composite function of the network layers ϕ_n , as defined in Eq. (7) as follows:

$$f_{\text{PIRes}}(\mathbf{w}, \mathbf{x}) = (H_R \circ H_{R-1} \circ \dots \circ H_r \circ \dots \circ H_1)(\mathbf{x}), \quad (10)$$

$$H_r = \frac{1}{2} \sin(\omega_0(\phi_{2r-1}(\mathbf{x}_{2r-1})\mathbf{w}_{2r} + \mathbf{b}_{2r}) + \mathbf{x}_{2r-1}) \quad (11)$$

where H_r is the r -th residual block ($r = 1, \dots, R$), where $R = N/2$. Parameters \mathbf{w} and \mathbf{b} are the weights and biases of the network, respectively. ω_0 is a hyperparameter for sine activation, as defined in Eq. (7).

As part of the network and data initialization procedure, to ensure the training stability of this network, the input data are normalized to the range $[-1, 1]$, and the weights in each layer are initialized according to Eqs. (8) and (9), respectively.

Although SIRENs with residual connections have been proposed in conventional studies [42], our architecture is distinguished by a different input-injection point, namely, we add the input at a different stage of the network.

C. TRAINING PROCESSES

A model is constructed to estimate RIRs using the networks presented in Eqs. (6), (7), (10) and (11). The network architectures of the conventional and proposed methods are

illustrated in Fig. 2(c). It should be noted that although the conventional and proposed methods share the same training procedure, they differ in their underlying network architectures.

First, during the training phase, the inputs to the model consist of discretized time steps combined with two types of spatial coordinates. The first type is the coordinates of the measurement points, which are required to calculate Eq. (4). The second type comprises the coordinates of \tilde{M} randomly selected points within the estimation region, which are required to calculate Eq. (5). These inputs can be represented as follows:

$$\mathbf{x}_{\text{meas}} = [t_v, x_{\tilde{m}}, y_{\tilde{m}}, z_{\tilde{m}}] \quad \tilde{m} \in \tilde{\mathcal{M}}, v \in \mathcal{T}, \quad (12)$$

$$\mathbf{x}_{\text{est}}^{(k)} = [t_v, x_m^{(k)}, y_m^{(k)}, z_m^{(k)}] \quad m \in \mathcal{M}, v \in \mathcal{T}, \quad (13)$$

where \mathbf{x}_{meas} is the input used to compute Eq. (4), which consists of the discretized time sample t_v and the coordinates of the measurement point $(x_{\tilde{m}}, y_{\tilde{m}}, z_{\tilde{m}})$. The other input, $\mathbf{x}_{\text{est}}^{(k)}$, is used to compute Eq. (5), and consists of the discretized time sample t_v and the coordinates of the estimation point (x_m, y_m, z_m) . The estimation coordinates are updated at each iteration, where k is the iteration index.

Both inputs, \mathbf{x}_{meas} and $\mathbf{x}_{\text{est}}^{(k)}$, are fed into the network. The outputs \hat{h}_m denote the RIRs at the discretized time sample and spatial coordinates. The MSE, Eq. (4), is calculated using the output \hat{h}_m corresponding to \mathbf{x}_{meas} . In addition, the wave equation is computed using the output \hat{h}_m corresponding to $\mathbf{x}_{\text{est}}^{(k)}$. To compute the wave equation, the temporal and spatial derivatives of output \hat{h}_m corresponding to $\mathbf{x}_{\text{est}}^{(k)}$ are calculated.

Backpropagation is then performed using the total loss function \mathcal{L} , Eq. (3), which balances the MSE and wave equation loss. Thus, by incorporating the wave equation into the loss function alongside the MSE, the PINNs constrain the network output to adhere to the governing physical law. By enforcing the governing physical law through this wave equation loss \mathcal{L}_{pde} , the model can estimate the RIRs in the vicinity of the measurement points and suppress noise in the measured RIRs.

IV. EXPERIMENTAL SETUP

Simulation experiments were conducted to estimate the early part of RIRs from a limited number of microphone signals in a three-dimensional sound field. The experiments aimed to examine the impact of residual connections and network depth on estimation accuracy and to select an appropriate activation function. The estimation accuracies of the four methods were compared: three conventional methods—PINNs with SIREN (PINNs-SIREN), PINNs with the hyperbolic tangent function (PINNs-tanh), PINNs with the hyperbolic tangent function and residual connections (PINNs-tanh-Res)—, and PINNs incorporating SIREN with residual connections (PINNs-SIREN-Res, the proposed method). All the architectures were implemented using PyTorch (version 1.12.0).

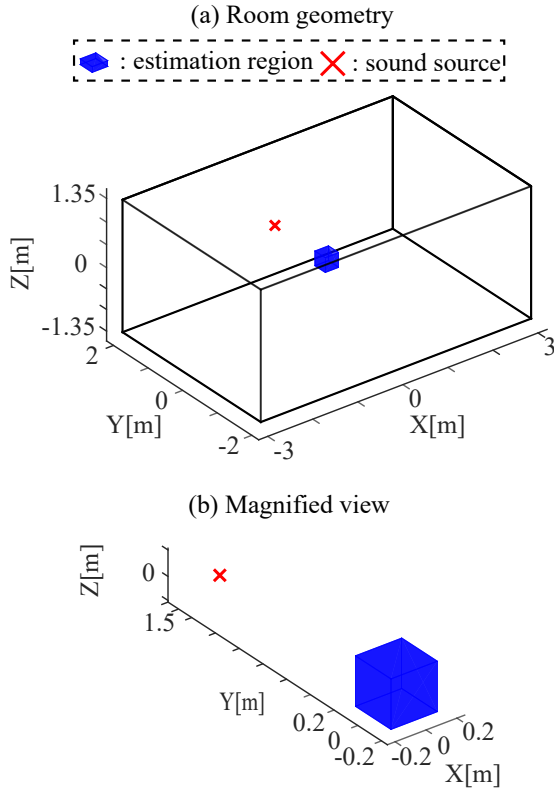


FIGURE 3: (a) Room geometry. (b) Magnified view of the estimation region and source position within the room. The sound source is positioned 1.5 m from the room's center in the positive y-direction. The estimation region is a 0.3 m cube, centered in the room. Microphones are placed within this estimation region, and the RIRs for this entire region are estimated from the measured signals. The evaluation points are defined by discretizing the estimation region into a $14 \times 14 \times 14$ grid.

A. SIMULATION SETUP

Figs. 3 and 4 show the room geometry, estimation region, and arrangement of the measurement points used in this experiment.

As shown in Fig. 3, the room geometry for the simulation was $6.0 \times 4.0 \times 2.7 \text{ m}^3$, and a point source was placed at (0, 1.5, 1.35). Following the conditions reported in a publicly available RIR dataset [44], the wall reflection coefficient was set to achieve a $T_{60} = 0.38 \text{ s}$. The estimation region was $0.3 \times 0.3 \times 0.3 \text{ m}^3$ and was positioned at the center of the room.

RIRs were simulated using the image source method [45] with the SFS-toolbox [46], considering reflections up to the fourth order. The simulated signals had a length of 400 samples and a sampling frequency of 8000 Hz. To simulate realistic measurement conditions, white noise was added to the measured signals to achieve a signal-to-noise ratio (SNR) of 20 dB.

As shown in Fig. 4, the measurement points were arranged equidistantly on a spherical surface. The total number of microphones was $M = 100$, with a radius of 0.15 m, and the microphone spacing was approximately 0.05 m. The sphere

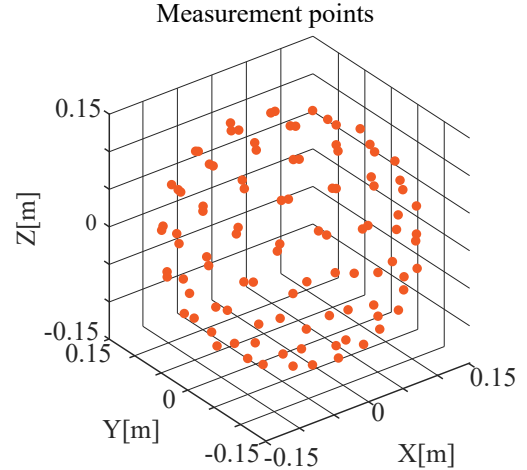


FIGURE 4: Arrangement of the measurement points. The points are positioned equidistantly with a 0.05 m spacing on a sphere with a radius of 0.15 m. The center of the sphere coincides with the center of the room.

was centered at the room center, which was considered as the origin (0, 0, 0).

B. NETWORK PARAMETERS

For all methods, we constructed models with $N = 6, 10, 14$ and 18 layers using $s_n = 256$ neurons in each hidden layer. By comparing networks of different depths, we evaluated the effect of depth and assessed whether deeper architectures improve performance relative to shallower ones.

These networks were trained for 50,000 iterations using the Adam optimizer. At each iteration, $\tilde{M} = 100$ random points were sampled for training. The learning rate was initialized at 1.0×10^{-4} and exponentially decayed by a factor of 0.98 every 100 iterations, to a final value of 1.0×10^{-6} .

The hyperparameter ω_0 and balance parameter λ were set to $\omega_0 = 7$ and $\lambda = 1.0 \times 10^{-6}$, respectively. Note that ω_0 and weight initialization (defined in Eqs. (8) and (9)) were only applied to the PINNs-SIREN and PINNs-SIREN-Res models.

C. EVALUATION METHOD

The estimation region was discretized into a $14 \times 14 \times 14$ grid, yielding $M_{eval} = 2744$ evaluation points. The coordinates of grid points were fed into each trained model to estimate the RIR at the corresponding positions. The estimation accuracy was evaluated using the normalized mean squared error (NMSE), defined as follows:

$$NMSE = 10 \log_{10} \sum_{m=1}^{M_{eval}} \sum_{v=1}^T \frac{\|h_m(t_v) - \hat{h}_m(t_v)\|_2^2}{\|h_m(t_v)\|_2^2}. \quad (14)$$

$h_m(t_v)$ and $\hat{h}_m(t_v)$ denote m -th ground truth and m -th estimated RIR, respectively. $v (= 1, \dots, T = 400)$ denotes time index. The evaluation was conducted using noise-free RIRs as the ground truth to compute the NMSE.

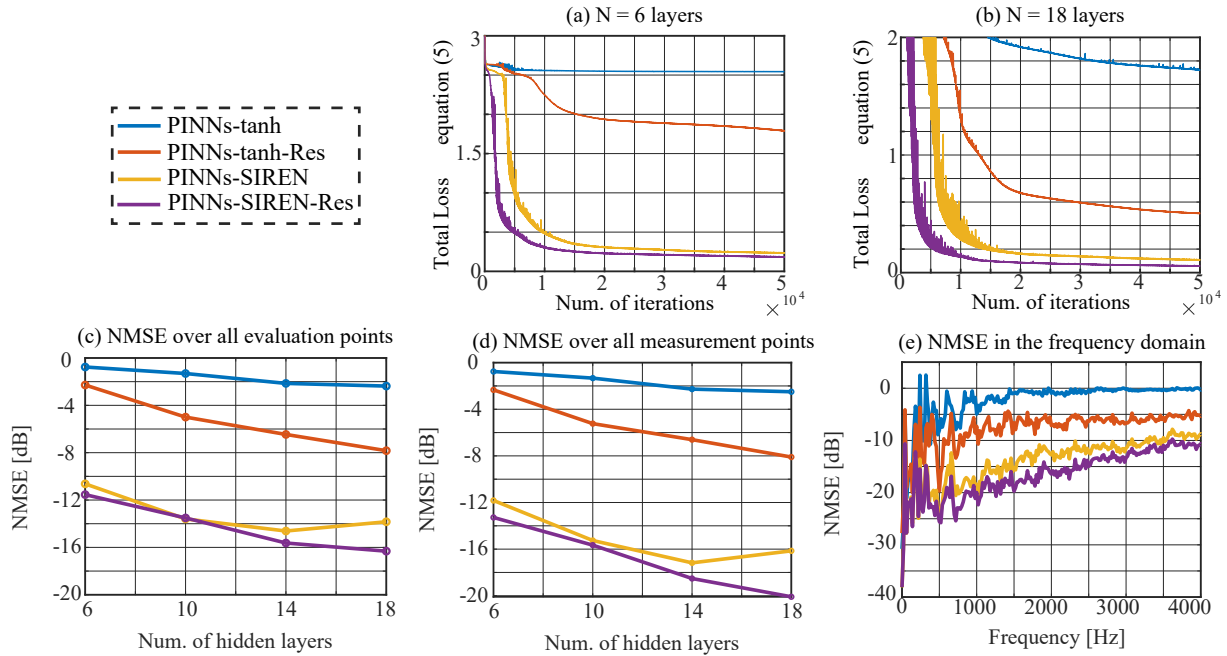


FIGURE 5: The trajectory of the loss function and estimation accuracy of evaluation and measured points. (a) The trajectory of the loss function \mathcal{L} over iterations for models with $N = 6$ hidden layers. (b) The trajectory of the loss function \mathcal{L} over iterations for models with $N = 18$ hidden layers. (c) NMSE of evaluation points versus the number of hidden layers. (d) NMSE of measurement points versus the number of hidden layers. (e) Frequency-domain NMSE for the best-performing model of each method, where the network depth is selected to maximize performance.

V. RESULTS

A. EVALUATION OF OVERALL ESTIMATION ACCURACY

In this section, we evaluate the proposed method in terms of training stability and estimation accuracy over the entire estimation domain.

1) Training Stability and Convergence

First, we examine the training stability and the convergence of models. Figs. 5(a) and (b) illustrate the trajectories of the total loss function \mathcal{L} over training iterations for models with $N = 6$ and $N = 18$ hidden layers, respectively.

As shown in Fig. 5(a), the total loss function converges successfully for the $N = 6$ model. Regarding the activation functions, PINNs-SIREN and PINNs-SIREN-Res converged more rapidly and stably than PINNs-tanh and PINNs-tanh-Res. Overall, the SIREN-based models showed consistently better convergence behavior than the tanh-based models, suggesting that SIREN can be advantageous for modeling acoustic wave propagation in this setting.

Within each activation function, incorporating residual connections led to faster and more stable convergence. This suggests that residual connections can accelerate training and improve the convergence behavior even for shallow networks. In particular, comparing PINNs-SIREN with PINNs-SIREN-Res, the residual variant achieved a slightly lower final loss after 50,000 iterations, indicating that the benefit

TABLE 1: NMSE [dB] of the lowest-NMSE model across the tested depths for each method with 50,000 training iterations. This table presents the Normalized Mean Squared Error (NMSE) values achieved after 50,000 iterations for each model (PINNs-tanh, PINNs-tanh-Res, PINNs-SIREN, and PINNs-SIREN-Res).

PINNs-tanh	PINNs-tanh-Res	PINNs-SIREN	PINNs-SIREN-Res
-2.1	-7.8	-14.6	-16.3

of the residual connections is observable even at $N = 6$. Overall, the proposed method achieved faster convergence and a lower final loss than its non-residual counterpart at shallow depth.

Fig. 5(b) shows the results for the deeper models ($N = 18$). The total loss \mathcal{L} converges for all methods. Consistent with the $N = 6$ case, PINNs-SIREN-Res achieved the fastest and most stable convergence, reaching the lowest loss among the compared models. In addition, within each activation function, the residual variants converged faster and attained lower final losses than their non-residual counterparts. Overall, the convergence-speed trends observed for $N = 6$ are preserved at $N = 18$.

From these results, the loss converged for all the methods, even for a deeper setting ($N = 18$). Across both depths, the SIREN-based models consistently converged faster and to lower loss values than the tanh-based models, and incorporating residual connections further improved the convergence, particularly in terms of speed and final loss.

TABLE 2: NMSE [dB] in each frequency band for the evaluated models.

Frequency Range [Hz]	PINNs-tanh	PINNs-tanh-Res	PINNs-SIREN	PINNs-SIREN-Res
0 – 1000	-8.2	-13.2	-23.2	-24.6
1000 – 2000	-1.5	-6.7	-15.5	-17.9
2000 – 3000	-0.6	-6.3	-12.8	-14.5
3000 – 4000	-0.3	-5.7	-10.1	-11.5

2) Estimation Accuracy over the Entire Evaluation Region

To clarify the effect of network depth on estimation performance, we compare the mean NMSE across all evaluation points. Fig. 5(c) shows the relationship between NMSE and the number of hidden layers ($N = 6, 10, 14, 18$), and Table 1 lists the NMSE of the lowest-NMSE model across the tested depths for each method.

First, for the tanh-based models, PINNs-tanh showed little improvement as depth increased: the NMSE was approximately -1.0 dB at $N = 6$ and -2.7 dB at $N = 18$. In contrast, PINNs-tanh-Res improved markedly with depth, reaching an overall NMSE of approximately -7.9 dB at $N = 18$, which is a 5.2 dB improvement over PINNs-tanh. Moreover, increasing the depth from $N = 6$ to $N = 18$ improved the NMSE of PINNs-tanh-Res by approximately 6.0 dB. These results indicate that residual connections are important for effectively exploiting increased depth in tanh-based PINNs.

Second, the results indicate that PINNs-SIREN achieves higher estimation accuracy than the tanh-based models among the compared models. For the best-performing models (across depths) of each type, PINNs-SIREN improved the NMSE by approximately 12.5 dB compared with PINNs-tanh and by 6.8 dB compared with PINNs-tanh-Res. As shown in Fig. 5(c), the NMSE of PINNs-SIREN improved as the depth increased up to $N = 14$; however, further increasing the depth to $N = 18$ led to a slight decrease in performance (approximately 0.6 dB). This suggests that PINNs-SIREN outperforms tanh-based models; however, its estimation accuracy may degrade beyond a certain depth.

Next, we evaluate the proposed method, PINNs-SIREN-Res. As summarized in Table 1, the best-performing model (across depths) achieves NMSE improvements of approximately 14.2 dB over PINNs-tanh, 8.5 dB over PINNs-tanh-Res, and 1.7 dB over PINNs-SIREN. Notably, while PINNs-SIREN showed a slight degradation when the depth was increased from $N = 14$ to $N = 18$, the proposed method instead improved the NMSE by 0.7 dB. These results indicate that the best-performing proposed model outperforms the corresponding best-performing conventional models, and that its estimation accuracy improves with increasing depth up to $N = 18$.

To assess the noise-reduction effect, Fig. 5(d) shows the mean NMSE at the measurement points. For all methods except PINNs-SIREN, the estimation accuracy improved with increasing depth. In contrast, PINNs-SIREN shows a decrease in accuracy when the network is deepened to $N = 18$. The proposed method improved the NMSE by approximately 17.6 dB compared with PINNs-tanh, 12.0 dB compared with

PINNs-tanh-Res, and 2.9 dB compared with PINNs-SIREN. Consistent with the trends observed at the evaluation points, these results indicate that the proposed method achieved the highest estimation accuracy at the measurement positions.

In the following sections, we compare the best-performing models for each method (in terms of network depth).

3) Frequency-Domain Accuracy

Fig. 5(e) shows the NMSE as a function of frequency. The figure indicates that all methods achieve lower NMSE (i.e., higher accuracy) at low frequencies than at high frequencies. In addition, fluctuations in NMSE are more pronounced in the low-frequency range across methods.

Compared with PINNs-tanh, PINNs-tanh-Res demonstrates improved estimation accuracy in the high-frequency range. The SIREN-based model further improves performance over the tanh-based models, and PINNs-SIREN-Res provides an additional gain, achieving the lowest NMSE overall. These results suggest that the proposed method improves estimation accuracy over a wide frequency range.

Table 2 summarizes the NMSE in four frequency bands: up to 1000 Hz, 1000 – 2000 Hz, 2000 – 3000 Hz, and 3000 – 4000 Hz.

PINNs-tanh attains an NMSE of -8.2 dB for frequencies up to 1000 Hz; however, its performance degrades substantially in higher bands compared with the other methods. For PINNs-tanh-Res, the NMSE increases by approximately 6.5 dB from the sub- 1000 Hz band to the 1000 – 2000 Hz band, but remains around -6 dB above 2000 Hz.

PINNs-SIREN achieves markedly better accuracy up to 1000 Hz (NMSE: -23.2 dB), but its NMSE gradually increases above 1000 Hz. The proposed PINNs-SIREN-Res achieves the best NMSE up to 1000 Hz (-24.6 dB) and shows less degradation than PINNs-SIREN at higher frequencies, indicating more stable estimation in the high-frequency bands.

Overall, the proposed method improves estimation accuracy across all frequency bands compared with the other methods. The general degradation at higher frequencies is likely due to shorter wavelengths, which make the wave field spatially more complex and therefore harder for the networks to resolve.

B. EVALUATION AT SPECIFIC POINTS

In this section, we evaluate the estimated signals and NMSE at specific evaluation points to analyze (i) the spatial accuracy inside and outside the microphone array (i.e., in the interior and exterior regions relative to the array) and (ii) the temporal accuracy of the estimates.

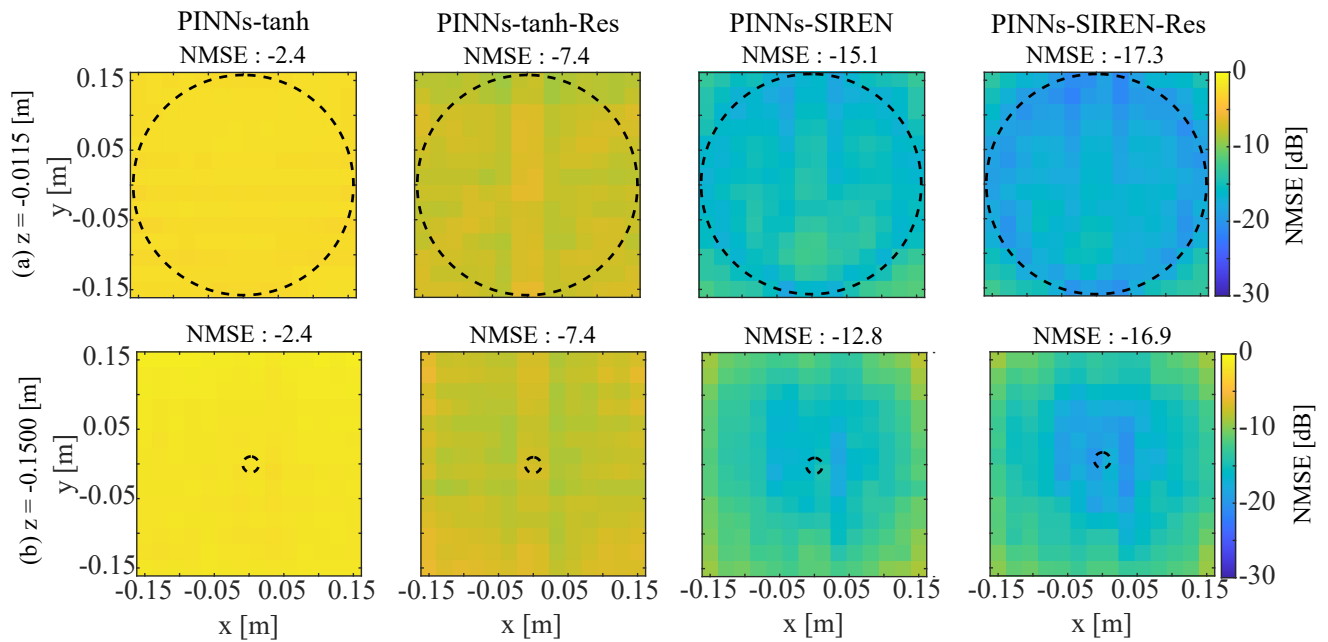


FIGURE 6: Spatial distribution of NMSE[dB] on two x-y plane: (a) the center plane ($z = -0.0115$ m) and (b) the bottom plane ($z = -0.1500$ m) of the discretized estimation region. The black dashed lines indicate the boundaries of the measurement region.

TABLE 3: NMSE [dB] in the interpolation and extrapolation regions (inside and outside the measurement sphere, respectively) for each model.

Estimated region	PINNs-tanh	PINNs-tanh-Res	PINNs-SIREN	PINNs-SIREN-Res
Interpolation	-2.5	-7.9	-15.6	-17.8
Extrapolation	-2.3	-7.8	-14.0	-15.5

1) Interpolation and Extrapolation Performance

We examined the spatial distribution of the estimation errors. Fig. 6 shows the spatial distribution of the NMSE over the evaluation points in the x-y plane.

Fig. 6(a) corresponds to the plane at $z = -0.0115$ m, which is the central slice of the evaluation domain along the z-axis. Note that, on this x-y plane, the measurement sphere is close to the boundary of the evaluation domain; consequently, many measurement points are concentrated near the periphery of the evaluation domain. Therefore, this slice is representative of interpolation performance. As shown in the figure, PINNs-tanh and PINNs-tanh-Res generally yielded a higher NMSE (i.e., lower accuracy) than the SIREN-based models across the evaluation points. The proposed method reduces the NMSE by approximately 14.9 dB, 9.9 dB, and 2.2 dB compared with PINNs-tanh, PINNs-tanh-Res, and PINNs-SIREN, respectively.

Moreover, within each activation-function family, introducing residual connections improved the accuracy. Notably, PINNs-SIREN-Res achieved the lowest NMSE among all models, indicating a strong interpolation performance.

Fig. 6(b) shows the evaluation points at $z = -0.1500$ m, corresponding to the bottommost layer of the evaluation domain. Because this layer lies on the boundary of the estimation domain, almost the entire plane falls within the extrapolation region; thus, this slice was used to evaluate the

extrapolation accuracy. Similar to Fig. 6(a), PINNs-tanh and PINNs-tanh-Res yielded a higher NMSE (lower accuracy) than the SIREN-based models. Consistent with the results for the central plane ($z = -0.0115$ m), the proposed method achieved the best accuracy at this depth.

Table 3 summarizes the NMSE for the evaluation points located inside (interpolation region) and those outside (extrapolation region) the measurement points. In the interpolation region, the proposed method reduced the NMSE by approximately 15.3 dB relative to PINNs-tanh, 9.9 dB relative to PINNs-tanh-Res, and 2.2 dB relative to PINNs-SIREN. In the extrapolation region, it reduced the NMSE by approximately 13.2 dB, 7.7 dB, and 1.5 dB compared with these methods, respectively. These results suggest that incorporating residual connections improved the estimation accuracy in both interpolation and extrapolation.

2) Time-Domain Analysis of Estimation Accuracy

We evaluated the estimated RIRs in the time domain by focusing on direct sound and reflected components. Fig. 7 shows a comparison of the RIRs and frequency responses at the $(x, y, z) = (-0.0115, -0.0115, -0.0115)$ m. In Fig. 7(a), PINNs-tanh failed to estimate the amplitude of the direct sound. As shown in Fig. 7(b), although PINNs-tanh-Res captures the amplitude of the direct sound, it failed to capture the amplitude of the first-order reflections and was

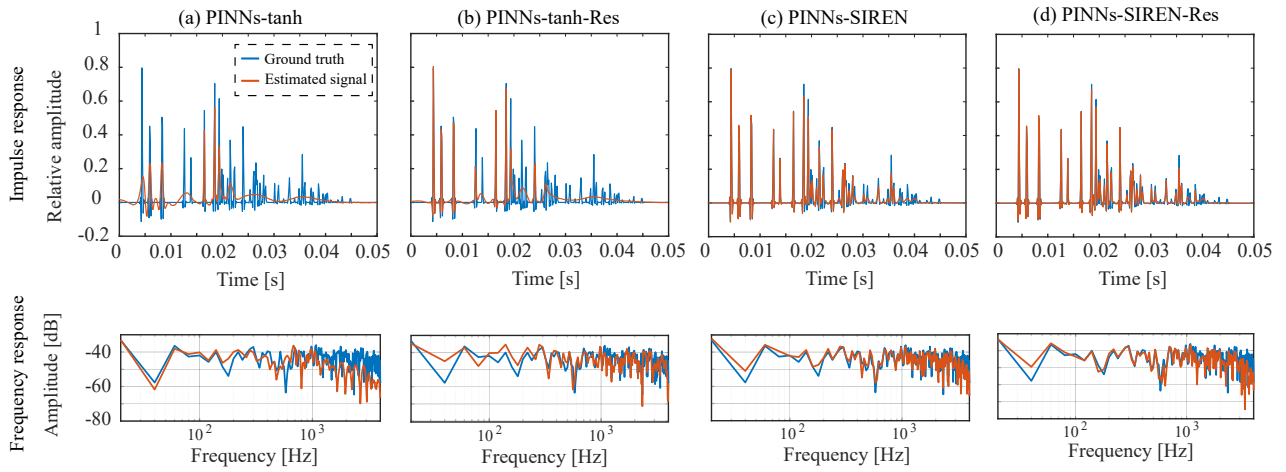


FIGURE 7: Estimated impulse response and frequency response at $(x, y, z) = (-0.0115, -0.0115, -0.0115)$ m, comparing each model’s estimates with the ground truth.

TABLE 4: NMSE [dB] for the early and late segments of the RIR. This table lists the NMSE for each model for the early segment (direct sound and early reflections) and the late segment (late reverberation). The late segment is defined as the portion of the RIR after 0.025 s.

Estimated region	PINNs-tanh	PINNs-tanh-Res	PINNs-SIREN	PINNs-SIREN-Res
Early segment	-2.4	-9.3	-18.0	-19.0
Late segment	-1.8	-2.3	-6.9	-9.2

similar to PINNs-tanh and could not reliably estimate the subsequent reflections. In contrast, the SIREN-based models in Fig. 7(c) and (d) capture the latter part of the RIR more effectively than tanh-based models. Moreover, a comparison of Figs. 7(c) and (d) indicates that PINNs-SIREN-Res estimates the late-reverberation tail more accurately than PINNs-SIREN.

Despite adding white noise to the measured signals at an SNR of 20 dB, the RIR estimated by the proposed method closely matched the ground truth. Notably, the estimated signal did not exhibit white-noise-like fluctuations, indicating a low sensitivity to noise. This characteristic is particularly evident in the time range before 0.025 s. These observations demonstrate the robustness of the proposed method against noise.

Table 4 presents the NMSE results segmented by time, distinguishing between the early and late portions of the signal (before and after 0.025 s) at all the evaluation points. In the early segment, the proposed method improves the NMSE by approximately 16.6 dB and 9.7 dB relative to PINNs-tanh and PINNs-tanh-Res, respectively. Even compared with the strong baseline of PINNs-SIREN, an improvement of 1.0 dB is achieved. In the late segment, the proposed method also maintains superior performance, improving the NMSE by approximately 7.4 dB, 6.9 dB, and 2.3 dB compared with PINNs-tanh, PINNs-tanh-Res, and PINNs-SIREN, respectively. Overall, these results indicate that SIREN-based models provide strong accuracy through the early-reflection

region, and that residual connections further improve the estimation of late-reverberation components.

VI. CONCLUSION

This study proposed a three-dimensional RIR estimation method based on PINNs with SIREN, incorporating deep hidden layers and residual connections (PINNs-SIREN-Res). The experimental results demonstrate that the proposed method achieves higher estimation accuracy and improved robustness than models using other activation functions. In particular, the improvement in the accuracy of the reflection components was remarkable.

Furthermore, whereas PINNs-SIREN exhibited performance degradation when the number of layers was increased from 14 to 18, the proposed method continued to improve with increased depth. The proposed method also outperformed PINNs-SIREN in estimating reflection components. In the frequency domain, consistent improvements were observed across all frequency bands, although the estimation accuracy degraded as the frequency increased for all methods.

Future work includes refining the model to improve estimation accuracy over a broader spatial domain, enhancing performance at higher frequencies, and improving the estimation of late reverberation. In addition, although this study validated the proposed method through simulation experiments, extending it to real-world measurements and practical acoustic environments is an important direction for future research.

REFERENCES

- [1] O. Kirkeby and P. A. Nelson, "Reproduction of plane wave sound fields," *The Journal of the Acoustical Society of America*, vol. 94, no. 5, pp. 2992–3000, 1 Nov. 1993.
- [2] G. N. Lilis, D. Angelosante and G. B. Giannakis, "Sound Field Reproduction using the Lasso," *IEEE Transactions on Audio, Speech, and Language Processing*, vol. 18, no. 8, pp. 1902–1912, Nov. 2010.
- [3] P. A. Grumiaux, S. Kitić, L. Girin, and A. Guérin, "A survey of sound source localization with deep learning methods," *The Journal of the Acoustical Society of America*, vol. 152, no. 1, pp. 107–151, 1 Jul. 2022.
- [4] D. Salvati, C. Drioli and G. L. Foresti, "Sound source and microphone localization from acoustic impulse responses," *IEEE Signal Processing Letters*, vol. 23, no. 10, pp. 1459–1463, Oct. 2016.
- [5] T. Gotoh, Y. Kimura, A. Kurahashi, and A. Yamada, "A consideration of distance perception in binaural hearing," *The Journal of the Acoustical Society of Japan*, vol. 33, no. 12, pp. 667–671, Dec. 1977.
- [6] J. D. Maynard, E. G. Williams, Y. Lee, "Nearfield acoustic holography: I. Theory of generalized holography and the development of NAH," *The Journal of the Acoustical Society of America*, vol. 78, no. 4, pp. 1395–1413, 1 Oct. 1985.
- [7] K. Yatabe and Y. Oikawa, "PDE-based interpolation method for optically visualized sound field," in 2014 IEEE International Conference on Acoustics, Speech and Signal Processing (ICASSP), pp. 4738–4742, 2014.
- [8] A. Uchida, I. Tsunokuni, Y. Ikeda, and Y. Oikawa, "Mixed reality visualization of room impulse response map using room geometry and physical model of sound propagation," in ACM SIGGRAPH 2023 Posters (SIGGRAPH '23), Article 20, pp.1–2, 2023.
- [9] S. M. Kuo and D. R. Morgan, "Active noise control: A tutorial review," in *Proceedings of the IEEE*, vol. 87, no. 6, pp. 943–973, Jun. 1999.
- [10] D.P. Yang, R.C. Wang, X.M. Zhang, H.B. Yang, M. Xu, H.Y. Yue, and Z.F. Liu, "Auxiliary active noise control system based on signal reconstruction," *Mechanical Systems and Signal Processing*, vol. 212, p. 111287, 2024.
- [11] Y. Suzuki, I. Tsunokuni and Y. Ikeda, "Sound field reproduction by higher-order mode matching based on equivalent source method," *IEICE Transactions on Fundamentals of Electronics, Communications and Computer Sciences*, vol. E108.A, no. 10, pp. 1401–1405, 2025.
- [12] D. L. Donoho, "Compressed sensing," *IEEE Transactions on Information Theory*, vol. 52, no. 4, pp. 1289–1306, Apr. 2006.
- [13] E. J. Candes, and M. B. Wakin, "An introduction to compressive sampling," *IEEE Signal Processing Magazine*, vol. 25, 2, pp. 21–30, Mar. 2008.
- [14] S. A. Verburg and E. Fernandez-Grande, "Reconstruction of the sound field in a room using compressive sensing," *The Journal of the Acoustical Society of America*, vol. 143, 6, pp. 3770–3779, 2018.
- [15] G. H. Koopmann, L. Song, and J. B. Fahnlne, "A method for computing acoustic fields based on the principle of wave superposition," *The Journal of the Acoustical Society of America*, vol. 86, 6, pp. 2433–2438, Dec. 1989.
- [16] E. Fernandez Grande, A. Xenaki, and P. Gerstoft, "A sparse equivalent source method for near-field acoustic holography," *Journal of the Acoustical Society of America*, vol. 141, 1, pp. 532–542, Jan. 2017.
- [17] I. Tsunokuni, K. Kurokawa, H. Matsuhashi, Y. Ikeda, and N. Osaka, "Spatial extrapolation of early room impulse responses in local area using sparse equivalent sources and image source methods," *Applied Acoustics*, vol. 179, p. 108027, 2021.
- [18] S. Koyama, and L. Daudet, "Sparse Representation of a Spatial Sound Field in a Reverberant Environment," *IEEE Journal of Selected Topics in Signal Processing*, vol. 13, no. 1, pp. 172–184, Mar. 2019.
- [19] R. Horiuchi, S. Koyama, J. G. C. Ribeiro, N. Ueno, and H. Saruwatari, "Kernel Learning for Sound Field Estimation with L1 and L2 Regularizations," 2021 IEEE Workshop on Applications of Signal Processing to Audio and Acoustics (WASPAA), p. 261–265, 2021.
- [20] N. Ueno, S. Koyama, and H. Saruwatari, "Kernel Ridge Regression with Constraint of Helmholtz Equation for Sound Field Interpolation," in 2018 16th International Workshop on Acoustic Signal Enhancement (IWAENC), pp. 436–440, 2018.
- [21] J. G. C. Ribeiro, S. Koyama, R. Horiuchi and H. Saruwatari, "Sound Field Estimation Based on Physics-Constrained Kernel Interpolation Adapted to Environment," *IEEE/ACM Transactions on Audio, Speech, and Language Processing*, vol. 32, pp. 4369–4383, 2024.
- [22] A. Krizhevsky, I. Sutskever, and G. E. Hinton, "ImageNet classification with deep convolutional neural networks," in *Proceedings of the 26th International Conference on Neural Information Processing Systems - Volume 1*, pp. 1097–1105, 2012.
- [23] I. Goodfellow, J. Pouget-Abadie, M. Mirza, B. Xu, D. Warde-Farley, S. Ozair, A. Courville, and Y. Bengio, "Generative adversarial networks," *Communications of the ACM*, vol. 63, no. 11, pp. 139–144, Nov. 2020.
- [24] F. Lluís, P. Martínez-Nuevo, M. B. Møller, and S. E. Shepstone, "Sound field reconstruction in rooms: Impainting meets super-resolution," *The Journal of the Acoustical Society of America*, vol. 148, no. 2, pp. 649–659, Aug. 2020.
- [25] E. Fernandez-Grande, X. Karakonstantis, D. CaviedesNozal, and P. Gerstoft, "Generative models for sound field reconstruction," *The Journal of the Acoustical Society of America*, vol. 153, no. 2, pp. 1179–1190, Feb. 2023.
- [26] O. Ronneberger, P. Fischer, and T. Brox, "U-Net: Convolutional networks for biomedical image segmentation," in *Medical Image Computing and Computer-Assisted Intervention – MICCAI 2015*, pp. 234–241, Nov. 2015.
- [27] M. Raissi, P. Perdikaris, and G. Karniadakis, "Physics-informed neural networks: A deep learning framework for solving forward and inverse problems involving nonlinear partial differential equations," *Journal of Computational Physics*, vol. 378, pp. 686–707, 2019.
- [28] S. Alkhadhr, X. Liu, and M. Almekkawy, "Modeling of the forward wave propagation using physics-informed neural networks," in 2021 IEEE International Ultrasonics Symposium (IUS), pp. 1–4, 2021.
- [29] V. Sitzmann, J. N. P. Martel, A. W. Bergman, D. B. Lindell, and G. Wetzstein, "Implicit neural representations with periodic activation functions," in *Proceedings of the 34th International Conference on Neural Information Processing Systems*, 2020.
- [30] F. Rosenblatt, "The perceptron: A probabilistic model for information storage and organization in the brain," *Psychological Review*, vol. 65, no. 6, pp. 386–408, 1958.
- [31] S. Koyama, J. G. C. Ribeiro, T. Nakamura, N. Ueno and M. Pezzoli, "Physics-informed machine learning for sound field estimation: Fundamentals, state of the art, and challenges," *IEEE Signal Processing Magazine*, vol. 41, no. 6, pp. 60–71, Nov. 2024.
- [32] M. Pezzoli, F. Antonacci, and A. Sarti, "Implicit neural representation with physics-informed neural networks for the reconstruction of the early part of room impulse responses," in *Proceedings of the 10th Convention of the European Acoustics Association Forum Acusticum 2023*, pp. 2177–2184, 2023.
- [33] X. Karakonstantis and E. Fernandez-Grande, "Room impulse response reconstruction using physics-constrained neural networks," in *Proceedings of the 10th Convention of the European Acoustics Association Forum Acusticum 2023*, pp. 3181–3188, 2023.
- [34] M. Olivieri, X. Karakonstantis, M. Pezzoli, F. Antonacci, A. Sarti, and E. Fernandez-Grande, "Physics-informed neural network for volumetric sound field reconstruction of speech signals," *EURASIP Journal on Audio, Speech, and Music Processing*, vol. 2024, Sep. 2024.
- [35] I. Tsunokuni, G. Sato, Y. Ikeda, and Y. Oikawa, "Spatial extrapolation of early room impulse responses with noise-robust physics-informed neural network," *IEICE Transactions on Fundamentals of Electronics, Communications and Computer Sciences*, vol. E107-A, no. 9, pp. 1556–1560, Sep. 2024.
- [36] R. Tian, P. Kou, Y. Zhang, M. Mei, Z. Zhang, and D. Liang, "Residual-connected physics-informed neural network for anti-noise wind field reconstruction," *Applied Energy*, vol. 357, p. 122439, 2024.
- [37] K. He, X. Zhang, S. Ren, and J. Sun, "Deep residual learning for image recognition," in 2016 IEEE Conference on Computer Vision and Pattern Recognition (CVPR), pp. 770–778, 2016.
- [38] G. Huang, Z. Liu, and K. Q. Weinberger, "Densely connected convolutional networks," in 2017 IEEE Conference on Computer Vision and Pattern Recognition (CVPR), pp. 2261–2269, 2017.
- [39] C. Cheng and G. Zhang, "Deep learning method based on physics informed neural network with resnet block for solving fluid flow problems," *Water*, vol. 13, no. 4, p. 423, 2021.
- [40] F. Jiang, X. Hou, J. Ye, and M. Xia, "Deeper-PINNs: Unlocking the power of deep physics-informed neural networks," *Applied Soft Computing*, vol. 185, p. 114048, Dec. 2025.
- [41] S. Wang, B. Li, Y. Chen, and P. Perdikaris, "PirateNets: Physics-informed deep learning with residual adaptive networks," *Journal of Machine Learning Research*, vol. 25, no. 1, 2024.
- [42] Y. Lu, K. Jiang, J. A. Levine, and M. Berger, "Compressive neural representations of volumetric scalar fields," *Computer Graphics Forum*, vol. 40, no. 3, pp. 135–146, 2021,

- [43] K. Kurata, G. Sato, I. Tsunokuni, and Y. Ikeda, "Noise-robust estimation of early-part room impulse responses based on physics-informed neural network with dynamic pulling method," in 2024 Asia Pacific Signal and Information Processing Association Annual Summit and Conference (APSIPA ASC), pp. 1–5, 2024.
- [44] S. Koyama, T. Nishida, K. Kimura, T. Abe, N. Ueno, and J. Brunnström, "MESHRIR: A dataset of room impulse responses on meshed grid points for evaluating sound field analysis and synthesis methods," in 2021 IEEE Workshop on Applications of Signal Processing to Audio and Acoustics (WASPAA), pp. 1–5, 2021.
- [45] R. Scheibler, E. Bezzam, and I. Dokmanić, "Pyroomacoustics: A python package for audio room simulation and array processing algorithms," in 2018 IEEE International Conference on Acoustics, Speech and Signal Processing (ICASSP), pp. 351–355, 2018.
- [46] H. Wierstorf and S. Spors, "Sound field synthesis toolbox," in 132nd Convention of the Audio Engineering Society, 2012.

...